Ocean stratification and low melt rates at the Ross Ice Shelf grounding zone

Carolyn Branecky Begeman[1], Slawek M. Tulaczyk[1], Oliver J. Marsh[2], Jill A. Mikucki[3], Timothy P. Stanton[4], Timothy O. Hodson[5], Matthew R. Siegfried[6], Ross D. Powell[5], Knut Christianson[7], and Matt A. King[8].

[1]Department of Earth and Planetary Sciences, University of California, Santa Cruz, Santa Cruz, CA, USA.

[2]Gateway Antarctica, University of Canterbury, Christchurch, New Zealand.

[3]Department of Microbiology, University of Tennessee, Knoxville, TN, USA.

[4]Department of Oceanography, Naval Postgraduate School, Monterey, CA, USA.

[5]Department of Geology and Environmental Geosciences, Northern Illinois University, DeKalb, IL, USA.

[6]Department of Geophysics, Stanford University, Stanford, CA, USA.

[7]Department of Earth and Space Sciences, University of Washington, Seattle, WA, USA.

[8]Surveying and Spatial Sciences, School of Land and Food, University of Tasmania, Australia.

Corresponding author: Carolyn Begeman (cbraneck@ucsc.edu)

Key Points:

- The ocean cavity near the grounding zone of the Ross Ice Shelf is vertically stratified with a boundary layer freshened by ice melting.
- A tidally-mixed zone and tidal currents are absent from this 10 m thick ocean cavity in the flexure zone.
- The observed stratification and low current velocities result in low melt rates (7 cm yr^{-1}).

This article has been accepted for publication and undergone full peer review but has not been through the copyediting, typesetting, pagination and proofreading process which may lead to differences between this version and the Version of Record. Please cite this article as doi: 10.1029/2018JC013987

Abstract

Ocean-driven melting of ice shelves is a primary mechanism for ice loss from Antarctica. However, due to the difficulty in accessing the sub-ice-shelf ocean cavity, the relationship between ice-shelf melting and ocean conditions is poorly understood, particularly near the grounding zone, where the ice transitions from grounded to floating. We present the first borehole oceanographic observations from the grounding zone of the Ross Ice Shelf, Antarctica's largest ice shelf by area. Contrary to predictions that tidal currents near grounding zones mix the water column, we found that Ross Ice Shelf waters were vertically stratified. Current velocities at mid-depth in the ocean cavity did not change significantly over measurement periods at two different parts of the tidal cycle. The observed stratification resulted in low melt rates near this portion of the grounding zone, inferred from phase-sensitive radar observations. These melt rates were generally <10 cm yr^{-1}, which is lower than average for the Ross Ice Shelf (~20 cm yr^{-1}). Melt rates may be higher at portions of the grounding zone that experience higher subglacial discharge or stronger tidal mixing. Stratification in the cavity at the borehole site was prone to diffusive convection as a result of ice-shelf melting. Since diffusive convection influences vertical heat and salt fluxes differently than shear-driven turbulence, this process may affect ice-shelf melting and merits further consideration in ocean models of sub-ice-shelf circulation.

1 Introduction

Antarctic ice shelves presently lose over half of their mass by basal melting (Rignot et al., 2013). Although basal melting of floating ice has a small direct effect on sea level (Shepherd et al., 2010), the indirect effects of ice-shelf thinning can be significant by increasing the flux of grounded ice into the ocean (Pritchard et al., 2012), potentially driving grounding zone retreat (Schoof, 2007). Thus, ice-shelf melting is a key dynamic mechanism connecting ocean warming to future ice-sheet collapse and consequent sea-level rise (Pritchard et al., 2012). Understanding the relationship between ice-shelf melting and ocean conditions is essential for accurate projections of sea-level rise.

Ice-shelf basal melting is driven by the flux of heat from sub-ice-shelf cavity water masses to the ice-shelf base. On broad spatial scales, basal melt rates increase with the thermal driving, the difference between water temperature and the local pressure- and salinity-dependent ice freezing point. For example, high thermal driving (4 °C) in the Amundsen Sea drives high basal melt rates averaging ~15 m yr^{-1} (Rignot et al., 2013; Stanton et al., 2013), and low thermal driving (0.5 °C) in the Ross Sea drives basal melt rates averaging ~0.1 m yr^{-1} (Moholdt et al., 2014). However, several factors generate spatial variability in basal melt rates within regions under similar thermal driving. Stratification typically exists below ice shelves between colder, meltwater-rich water and warmer, denser continental shelf water (e.g., Jacobs et al., 1979). This stratification reduces the effective thermal driving. Meltwater from subglacial outflow or basal melting can generate a buoyant plume that entrains warmer seawater from below, driving high basal melt rates (e.g., Gladish et al., 2012; Jenkins, 2011). The effect of plume flow on melt rates tends to be greatest in magnitude and most localized (i.e., channelized) near the grounding zone (Dutrieux et al., 2013; Marsh et al., 2016).

Tidal variations in current velocity can also elevate turbulent heat fluxes to the ice shelf; these variations can be up to several times the mean current velocity below ice shelves

(e.g., Nicholls et al., 1997). Numerical modeling indicates that tides enhance ice-shelf melting and its spatial variability (Makinson et al., 2011; Mueller et al., 2012, 2018; Padman et al., 2018). Where the ocean cavity is narrow, as it is near the grounding zone, current shear at water mass boundaries enhanced by tides could be sufficient to destroy stratification (P. R. Holland, 2008; MacAyeal, 1984). A tidally-mixed zone prevents the formation of a meltwater plume close to the grounding zone, where subglacial discharge occurs (P. R. Holland, 2008). Thus, tidally-mixed zones may reduce the distance over which the plume accelerates, and consequently reduce the plume's velocity and turbulent entrainment of heat into the stratified layer. Tidally-mixed zones may also help buffer ice-shelf melt rates near the grounding zone from changes in sub-ice-shelf circulation (P. R. Holland, 2008; MacAyeal, 1984), of which the most concerning for ice-shelf stability has been the incursion of warm Circumpolar Deep Water (e.g., Cook et al., 2016).

The loss of grounded ice is particularly sensitive to ice-shelf melting near the grounding zone compared with ice-shelf melting elsewhere (Gagliardini et al., 2010; Reese et al., 2018; Walker et al., 2008). Despite this relationship, the thin sub-ice-shelf ocean cavity near grounding zones has rarely been observed, due to the logistical challenge of accessing these areas that tend to be far from the open ocean and beneath thick ice. Here we report on direct observations of the ocean cavity below the largest Antarctic ice shelf, the Ross Ice Shelf (RIS), near the Whillans Ice Stream grounding zone. To our knowledge, this is the first oceanographic study near the RIS grounding zone and the second oceanographic study near the grounding zone of an Antarctic ice shelf (Sugiyama et al., 2014). Past direct observations of the ocean cavity below the RIS have been limited to three borehole locations, one 200 km downstream of the grounding zone (Jacobs et al., 1979) and two within 20 km of the ice shelf front (Arzeno et al., 2014) (Figure 1a). The new borehole lies within the flexure zone, where the ice transitions from fully grounded to fully floating, as determined from TerraSAR-X data collected in 2012 (Figure 1b) (Marsh et al., 2016). We combine oceanographic observations with contemporaneous coherent radar measurements of basal melting to evaluate the relationship between ocean water properties and melt rates in a grounding zone setting and determine whether this setting is tidally mixed.

2 Methods

2.1 Oceanographic observations of the sub-ice shelf cavity

The Whillans Ice Stream Subglacial Access Research Drilling (WISSARD) field team accessed the sub-ice shelf cavity through a borehole drilled with hot water (Rack et al., 2014; Tulaczyk et al., 2014), and deployed geophysical instruments into the cavity during January 7-19, 2015. To maintain access during this period, the borehole was reamed once with hot water (Figure 2).

Current velocity and direction in the cavity were measured using a Nortek Aquadopp 2 MHz Acoustic Doppler Current Profiler (ADCP). This instrument was deployed once at low tide (ADCP1) and again at rising tide (ADCP2) as determined by a tide model and GPS observations (Figure 2). The ADCP has instrumental accuracy of 1% of the current magnitude ± 0.5 cm s^{-1} and 2° in current orientation. Since current variability is not expected on very short timescales, the average standard deviation of velocity measurements over 10-minute intervals is taken to be an in situ estimate of instrumental noise, equal to 0.2 cm s^{-1}. Acoustic backscatter levels were very weak due to low concentrations of suspended

particulate matter, resulting in limited range and high noise when collecting vertical current profiles. To improve the signal-to-noise ratio, measurements were made at 1 Hz then only the first range bin was low pass filtered at 2 mHz for an interval of 5-6 hours with the sensor stationed ~5 m below the ice shelf base near the middle of the water column. We only analyzed data collected when the ADCP was rotating less than 2° s^{-1} and the current orientation was changing less than 2° s^{-1} during intervals of at least 30 s.

A Sea-Bird Electronics 19plus V2 CTD profiler was used to measure conductivity (C), temperature (T) and depth (D; through pressure, P) at a frequency of 4 Hz with accuracies of 0.5 mS m^{-1}, 0.005 °C and 1 dbar, respectively. The three profiles are referred to as CTD1, CTD2 and CTD3 as labeled in Figure 2. Raw data are available as Data Set S1. The profiler was lowered at a (median) rate of 14.8 cm/s for CTD1, 4.1 cm/s for CTD2, and 8.6 cm/s for CTD3. We smooth the descent rate with a window of 2 s. Higher noise levels were particularly evident in CTD2 likely due to the very low descent speed of the sensor and small amplitude internal waves resulting in false apparent overturns in salinity. There is a period of temperature sensor error in CTD3 (Figure 3), which may be due to ice particles passing through the pumped sensor system.

We derive absolute salinity (SA), conservative temperature (Θ) and potential density (ρ) referenced to 665 dbar using the CTD data and the Thermodynamic Equation of Seawater (IOC et al., 2010). The accuracy of these derived quantities is 6 x 10^{-3} g kg^{-1}, 0.005 °C, and 4 x 10^{-4} kg m^{-3}, and the instrument resolution is 6 x 10^{-5} g kg^{-1}, 1 x 10^{-4} °C, and 1 x 10^{-4} kg m^{-3}, respectively though likely not consistently met during these observations.

The cavity top was identified by a sharp contrast in Θ and SA. The ice-shelf thickness is estimated to be 755 m from CTD-derived density profiles and laser-determined distance from ice-surface to the borehole water surface. The ice-shelf thickness is independently estimated to be 757 m by temperature sensors at 1 m intervals on a steel-reinforced cable of known length. The thickness of the sub-ice shelf cavity was determined by lowering the CTD instrument until it rested on the seafloor as determined by pressure maxima. Mixed layers within the observed stratification were defined by local gradients in filtered Θ that were less than the background thermal gradient (Table 2) over the 10-m-thick cavity for at least 0.5 m.

In order to characterize the observed stratification, we calculated the Turner angle, whose values differentiate double-diffusive, salt-fingering, statically stable, and statically unstable regimes:

$$Tu = \tan^{-1}(\beta_\Theta \Theta_z + \beta_{\mathrm{SA}} \mathrm{SA}_z, \beta_\Theta \Theta_z - \beta_{\mathrm{SA}} \mathrm{SA}_z) \quad (1)$$

where subscript z denotes the depth-derivative. $\beta_\Theta, \beta_{\mathrm{SA}}$ are the thermal expansion and saline contraction coefficients, which are 4 x 10^{-5} $°C^{-1}$ and 8 x 10^{-4} $(g/kg)^{-1}$ in this setting (IOC et al., 2010). We applied filtering methods to damp the influence of instrumental noise on the Turner angle. There is a tradeoff between noise reduction and steepness of gradients between mixed layers, particularly as the characteristics of instrumental noise are uncertain and inconsistent among the profiles. Thus, we settled on more conservative filtering that preserves scalar gradients as well as some instrumental noise. The T and C profiles of CTD1 and CTD3 were single-pole low-pass filtered at 2 s, and the profiles of CTD2, which had more noise, were filtered at 4 s. We low-pass filtered all casts at 1 s in P and smoothed the

descent rate with a window of 2 s. Θ_z and SA_z were calculated using linear least-squares over 20 cm intervals. We also calculate the inverse stability ratio,

$$R_\rho^* = \frac{\beta_{\mathrm{SA}} \Delta SA}{\beta_\Theta \Delta \Theta} \quad (2),$$

the inverse of the stability ratio defined by Ruddick (1983). ΔSA, $\Delta \Theta$ are salinity and temperature differences between mixed layers.The uppermost water layer of CTD1 is not analyzed because its salinity characteristics had not yet recovered from the perturbation of borehole opening. The temperature and salinity discontinuities at the ice base are small in CTD2 and CTD3 because we pumped water out of the borehole at a low rate prior to and during these casts. At the time of CTD2 and CTD3 water in the lower part of the borehole was at seawater salinity and had relaxed to the pressure- and salinity-dependent freezing point, which is the expected temperature at the ice shelf base when in thermodynamic equilibrium.

2.2 Ice shelf basal melt rates

We estimated ice-shelf basal melt rates at 11 locations in and around the grounding zone embayment using an Autonomous phase-sensitive Radio-Echo Sounding (ApRES) system following Brennan et al. (2013) and Marsh et al. (2016). At each site radar measurements were collected at weekly intervals over a period of 10-38 days with intermediate measurements used to validate mean melt rates over the entire period. Given that the ice shelf is ~755 m thick at the borehole, measurements represent basal melt rates over a 50-60 m diameter area.

The total thinning of the ice shelf between ApRES measurements includes both an internal vertical strain component and a melt component. The vertical strain is calculated by tracking the movement of internal layers within the upper 500 metres of the ice column. Internal reflectors are cross-correlated between shots to identify movement in range with a linear trend fitted to the whole ice column using iteratively re-weighted least-squares regression to remove the effect of outliers. After subtracting the strain, the remaining movement of the basal reflector is interpreted as basal melting. The basal reflector has a high signal to noise ratio implying a sharp change in dielectric properties at the ice base.

While flexure of the ice due to ocean tides influences how the strain rate varies through time, the strain remains relatively constant with depth. The derived melt rate is consistent between consecutive measurements (Table 2) and is independent of the varying strain rate. While melt rates of a few centimetres per year are close to the limit of detection over this time period, the measurements are significant relative to measurement error.

We compute the heat and salt fluxes associated with basal melting from the ApRES-derived basal melt rate at the borehole. Fluxes are defined as positive upward. The heat flux required to produce the observed basal melt rate is

$$Q_{melt}^T = \rho_i m' L_f \quad (1)$$

where ρ_i is the ice density taken to be 917 kg m^{-3}, m' is the melt rate, and L_f is the latent heat of fusion. There will be some conductive heat loss from the water at the ice shelf base; however, it will be small relative to the uncertainty in melt rates and is neglected here

(following Jenkins et al., 2010). We assume that salt fluxes into the ice are negligible. The salt flux induced by melting is

$$Q_{melt}^{S} = \rho_i m' S_{io} \quad (2)$$

where S_{io} is the salinity at the ice-ocean interface, assuming the salinity of basal shelf ice is 0 g kg^{-1}. Q_{melt}^{S} was calculated using S_{io} equal to salinity values found at the base of the ice borehole. Although S_{io} is not well-constrained due to the presence of the borehole, uncertainty in Q_{melt}^{S} is dominated by uncertainty in m' (99% of error determined by Gaussian propagation of errors from ApRES standard error and a plausible range of S_{io} values as established in Section 4.1).

The primary tool for modelling ice-shelf basal melting and freezing in both ocean models (Dansereau et al., 2013; Gwyther et al., 2016) and coupled ice-sheet ocean models (Jordan et al., 2018) is the "three-equation model." The three equations express the pressure- and salinity-dependent freezing point of water, heat conservation, and salt conservation at the ice-ocean interface (D. M. Holland & Jenkins, 1999). The key parameters in this model are the exchange velocities (γ_T, γ_S) that describe fluxes of heat and salt across the viscous sub-layer. We applied our observations of water properties and melt rates to compare several parameterizations of exchange velocity with respect to ice-shelf melt rates derived using the three-equation model.

The three equations are as follows:

1. Freezing temperature condition

$$T_{io} = c_1 + c_2 S_{io} + c_3 P_{io} \quad (3)$$

where T_{io} and P_{io} are the temperature and pressure at the ice-ocean interface and c_1, c_2, c_3 are the coefficients that describe the freezing point of freshwater at atmospheric pressure (0.081 °C), the salinity dependence of the freezing point (-0.0568 °C (g kg^{-1})$^{-1}$), and the pressure dependence of the freezing point (-7.61 x 10^{-4} °C m^{-1}), respectively (Jenkins, 2011). We set P_{io} from CTD data to the value at the cavity top. c_1, c_2 are chosen to fit the freezing point curve defined by the Thermodynamic Equation of Seawater at the pressure at the ice base over a plausible salinity range for the ice-ocean interface at this site (33.0 – 34.7 g kg^{-1}, see Section 4.1) (IOC et al., 2010).

2. Heat conservation

$$Q_{melt}^{T} = \rho_{UL} c_{pw} \gamma_T (T_{UL} - T_{io}) \quad (4)$$

where ρ_{UL} is the density of the upper layer (UL) water adjacent to the ice base, c_{pw} is the specific heat of water, γ_T is the heat exchange velocity, and T_{UL} is the temperature of UL water.

3. Salt conservation

$$Q_{melt}^{S} = \rho_{UL} \gamma_S (S_{UL} - S_{io}) \quad (5)$$

where γ_S is the salt exchange velocity, S_{UL} is the salinity of the UL water and, as before, heat conduction into the ice and salt diffusion into and out of the ice are neglected, as they are negligible compared to the melt rate term.

We use these three equations, oceanographic observations, and the observed basal melt rate to define the equivalent heat and salt exchange velocities (γ_T, γ_S) as a function of the salinity at the ice-ocean interface (S_{io}). We then use these calculated exchange velocities

to assess available parameterizations for exchange velocities. We test four parameterizations of exchange velocity: constant values (Hellmer & Olbers, 1989), a linear function of the friction velocity (Jenkins et al., 2010), and two other friction-velocity-dependent parameterizations (Kader & Yaglom, 1972; McPhee, 1983). The details of these parameterizations are summarized in D. M. Holland & Jenkins (1999). For the friction-velocity-dependent parameterizations, we solve for the friction velocity that produces the observationally constrained exchange velocity. We then use a quadratic drag relation for friction velocity, u^*, to solve for the far-field velocity, u

$$u^* = c_d^{1/2} u \quad (6)$$

where c_d is the drag coefficient. There are large uncertainties in the drag coefficient; we use a range from 0.001 to 0.01 (a commonly-used value is 0.003; see Jenkins et al. (2010)). The far-field velocity yielded by the exchange velocity parameterizations and the observed melt rate is then compared to the observed velocity at mid-depth in the water column.

A two-equation approach presents an advantage over the 3-equation parameterization in that it eliminates the unknown S_{io} (McPhee, 1992). In this approach, a single turbulent transfer coefficient, $\Gamma_{\{TS\}}$, represents the relative fluxes of heat and salt. Equation 3 is replaced with the freezing point evaluated at the far-field salinity

$$T_f = c_1 + c_2 S_{UL} + c_3 P_{io} \quad (7),$$

and Equation 4.4 is replaced with

$$Q_{melt}^T = \rho_{UL} c_{pw} u_* \Gamma_{\{TS\}} (T_f - T_{UL}) \quad (8).$$

We use these two equations to solve for the turbulent transfer coefficient $\Gamma_{\{TS\}}$ that fits our observations and compare it with previously derived values.

The inputs to the parameterization, T_{UL}, S_{UL} and ρ_{UL}, should be derived from the interval closest to the ice-shelf base where the water is fully turbulent. Given that the UL is well-mixed and thus likely to be turbulent, we set these values equal to their mean values within the UL. One could make the case that these input parameters should drawn from the shallowest depth at which the data fit a meltwater mixing line, which represents turbulent mixing between meltwater and seawater (further discussed in Section 3.1). If we use these properties as inputs to the parameterization, the predicted melt rates are about 20% higher than when the mean UL properties are used (Table 3).

2.3 Tidal forcing near the grounding zone

To quantify the local, non-hydrostatic, vertical motion of the ice shelf with tides, we collected continuous dual-frequency GPS data 284 m downstream of the borehole. The data were processed using Track v1.29 software (Chen, 1998) relative to a reference station (RAMG) located on bedrock 200 km away. We used final precise satellite orbits from the International GNSS Service to form the ionosphere-free linear combination of the two GPS frequencies. Antenna phase-center variations were modelled using igs08_1884.atx, and solid Earth tides were also modelled. Ocean tide loading displacements are small in this region and further cancel through differencing. Real-valued carrier-phase ambiguity parameters were fixed to integers where possible. Site coordinates and tropospheric zenith delays were estimated after applying a Kalman filter/smoother every measurement epoch (30s). Site coordinates and tropospheric zenith have process noise of 5 mm $(30s)^{-1/2}$ and 0.1 mm (30s) $^{-}$

$^{1/2}$, respectively. These temporal parameter constraints are loose enough not to over-smooth data or affect tidal frequencies while reducing noise. The short-term repeatability of the resulting vertical coordinate time series suggests a precision of 1-2 cm.

3 Results

3.1 Observations of ice-shelf melting

Basal melt rates were generally low in the grounding zone embayment (Figure 1b). Melt rates at seven sites were within 2 S.D. of 0 m yr^{-1}, so neither melting nor freezing can be confidently identified. For the four remaining sites, melt rates tend to increase with distance from the grounding zone, with the highest rate (60 ± 6 cm yr^{-1}, as mean ± 1 S.D.) observed at the farthest site from the grounding zone (10 km from the upstream flexure limit). Strain rates measured at these sites over 1-5 weeks range from -0.14 to 0.15 mm $m^{-1}yr^{-1}$.

The melt rate at the borehole was 7 ± 2 cm yr^{-1} over the full ApRES measurement period. We focus on the melt rate during the same period as oceanographic observations of 5 ± 2 cm yr^{-1}. This is equivalent to a heat flux of 0.49 ± 0.20 W m^{-2} and a salt flux of 50 ± 20 µg s^{-1} m^{-2}. We do not detect statistically-significant variations in basal melt rate on weekly timescales at the borehole site at the 95% confidence level (Table 1).

3.2 Oceanographic observations

Three direct observations of the vertical structure of ocean temperature and conductivity were collected over seven days through the borehole. These observations reveal double-diffusively-stable stratification within the 10 m thick sub-ice-shelf ocean cavity (Figure 3). Instrument noise is responsible for high frequency variability in temperature and salinity that produces the appearance of unstable stratification in these profiles, particularly in the lower half of the water column where mean gradients are small. Thus, we do not interpret the apparent gravitational instabilities shown in Figure 3c, as we do not believe them to be physical. When the high frequency variability is ignored, the observed stratification is also thermobarically stable (Akitomo, 1999).

The observed stratification was composed of three, 1-4 m thick mixed layers, an Upper Layer (UL), Middle Layer (ML) and Bottom Boundary Layer (BBL) as labeled in Figure 3. The interface between UL and ML is ~2.5 m thick and characterized by temperature gradients of ~0.1 °C m^{-1} and salinity gradients of ~0.06 g kg^{-1} m^{-1}. The interface between UL and ML is 1-2 m thick and characterized by weaker gradients in temperature and salinity, ~0.04 °C m^{-1} and ~0.006 g kg^{-1} m^{-1}. The interface close to the base of the borehole is considered a transition layer, whose steep temperature and salinity gradients influenced by borehole water properties.

The maximum thermal driving at the site is 0.1 °C, the difference between UL temperature and the minimum freezing temperature of -2.39 °C based on UL salinity(Figure 4b). In contrast, thermal driving is 0.35-0.50 °C for HSSW temperatures at the ice-shelf front at depths greater than 500 m (Orsi & Wiederwohl, 2009) relative to the same UL freezing temperature.

This stratification persisted over seven days, and its properties were generally consistent between observations (Table 2). Even though the water properties of CTD1 near

the ice-ocean interface may have been disturbed by borehole operations, the properties below UL were consistent between CTD1, CTD2, and CTD3. There was some variability in ML characteristics on sub-weekly timescales, with a maximum increase in ML temperature of 0.04 °C over 36 hours (between CTD2 and CTD3).

When the eddy diffusivities of heat and salt are identical ($k_s/k_t = 1$), the temperature and salinity characteristics will have the slope of the "meltwater mixing line" connecting source water temperature and salinity with meltwater properties. The slope of this line ($d\theta/dSA$) was originally defined by Gade (1979) and corrected by McDougall et al. (2014). We evaluate the hypothesis that heat and salt transport are fully turbulent using the meltwater mixing line fit to CTD properties. The source waters for the meltwater mixing lines are chosen at 666.3 dbar, the greatest depth before a break in θ-SA slope away from the meltwater mixing line. The CTD data most closely fits the meltwater mixing line over a ~0.5 m interval within the UL-ML interface using basal ice temperature at the freezing point (a slope of 2.37 °C (g/kg)$^{-1}$, Figure 4b). The fit between data and the meltwater mixing line is reduced if colder basal ice temperatures are used. The UL water mass diverges from the meltwater mixing line, at lower salinities and higher temperatures than the meltwater mixing line predicts. Two explanations for these characteristics are differential diffusion of heat over salt ($k_s/k_t < 1$) and lateral advection of UL. Warmer and fresher UL water could be produced by a mixture of locally-produced meltwater and subglacial meltwater, characterized by a higher freezing point (~0.5 °C), which is advected to this site. Furthermore, even if $k_s/k_t = 1$ at this site, advection of UL water from sites where $k_s/k_t < 1$ or where the source water characteristics differ could produce the observed characteristics. We discuss the possibility of differential diffusion in sections 4.1 and 4.3.b but cannot address the possibility of lateral advection as we do not have current profiles or information about water properties upstream or downstream.

Measured ML currents at ~5 m below the ice shelf were 1.5 ± 0.2 cm s^{-1} (mean ± 1 S.D.) oriented 175 ± 95° (mean ± 1 S.D.) during ADCP1 (falling tide) and 1.3 ± 0.3 cm s^{-1} oriented 165 ± 25° during ADCP2 (rising tide). Apparent current orientation fluctuates in ADCP1, as a result of sensor rotation in the water column. This sensor motion may induce fluid motion near the sensor that biases measurements of current velocity and orientation. Only short intervals of data from ADCP1 passed our criteria for reliable data of both low sensor rotation rates and low current rotation rates. Thus, current orientation over this period is not well-constrained. Current speeds were not significantly different at the two observed parts of the tidal cycle (Figure 5a). The tidal velocity variation between these two intervals is within 1 S.D. of 0 cm s^{-1} ($\overline{u}(\text{ADCP1}) - \overline{u}(\text{ADCP2}) = 0.2 \pm 0.4$ cm s^{-1}) and has an amplitude less than the mean current. Thus, at mid-depth in the sub-ice-shelf cavity there is a weak mean current oriented toward the grounding zone, with a weak or absent tidally-varying component.

3.3 Tidal motion of the ice shelf

The Ross Sea ocean tide is mainly diurnal, and variations in ice-shelf height at the borehole were about 40% of the predicted diurnal variations in the freely-floating ice shelf according to the CATS 2008a tidal model (after (Padman et al., 2002). During ADCP1, tides were falling to low tide during a neap tide with a freely-floating tidal range of 0.77 m and a local ice-shelf height change of 0.35 m. During ADCP2, tides were rising during a spring tide

with a freely-floating tidal range of 1.8 m and a local ice-shelf elevation change of 0.79 m. This was close to the maximum diurnal ice-shelf height change observed in January 2015 at the borehole site of 0.81 m. These reductions in vertical ice-shelf motion are consistent with the location of the borehole within the flexure zone near the grounding zone.

4 Discussion

4.1 Ice-shelf melting: effectiveness of parameterizations

Using observationally constrained ocean conditions we assess the consistency of observed melt rates with parameterizations used in two- and three-equation models. We directly assess the accuracy of the 3-equation, velocity-independent parameterization of Hellmer & Olbers (1989), which overestimates melt rates at this site by an order of magnitude (76 cm yr^{-1}). Other 3-equation parameterizations rely on a far-field velocity to estimate the friction velocity. Our current velocity measurement is located 5 m from the ice base and below a significant stratification layer, and so may not capture the appropriate far-field velocity for determining the friction velocity. These 3-equation, velocity-dependent parameterizations (Jenkins et al., 2010; Kader & Yaglom, 1972; McPhee, 1983) are consistent with the observed melt rates and drag coefficients of 0.001-0.01 for far-field velocities of 0.2-0.7 cm s^{-1}, 0.2-0.5 cm s^{-1}, and 1-3 cm s^{-1}, respectively (Table 3). These parameterizations suggest a slowly flowing UL. This is consistent with the low measured ice-shelf basal slopes (not significantly different from flat) in this grounding zone embayment (Horgan et al., 2013), which generate little buoyant acceleration.

The low melt rates also indicate a low turbulent transfer coefficient $\Gamma_{\{TS\}}$ in the two-equation model (Equations 6 and 7). We report $c_d^{1/2}\Gamma_{\{TS\}}$, called the Stanton number, using a far-field velocity of 1 cm s^{-1} (Table 3). This Stanton number estimate is 2 orders of magnitude lower than the Stanton number for sub-sea-ice turbulence (McPhee et al., 1999) and 1 order of magnitude lower than the previously mentioned sub-ice-shelf setting (Jenkins et al., 2010). Both a low Stanton number and the 3-equation, velocity-dependent parameterization solutions are only consistent with the low observed melt rates when the ratio of parameterized exchange velocities, γ_t/γ_s, greatly exceeds 1 (Figure 6c). These high ratios may indicate the dominance of molecular diffusion over turbulent exchange in the viscous sub-layer close to the ice-ocean interface.

4.2 Absence of a tidally-mixed zone

Although a tidally-homogenized zone has been postulated to develop near some ice-shelf grounding zones, stratification is observed 3 km from the Whillans Ice Stream grounding zone. While tides may play a role in homogenizing the BBL, it is notable that tidal forcing was insufficient to homogenize the relatively weak stratification between UL and ML. The observed oceanographic conditions and melt rates are consistent with a proposed threshold between stratification and full-water-column tidal mixing (MacAyeal, 1984). The threshold has been defined by melt rate at which turbulent kinetic energy dissipation is balanced by the potential energy needed to mix the freshwater supplied by ice-shelf melting through the entire water column (MacAyeal, 1984):

$$m_c = \frac{2\alpha c_d \langle |\boldsymbol{u}|^3 \rangle}{\beta_S g S h} \quad (9)$$

where α is the fraction of dissipated energy that goes into eroding stratification (assumed to be $\mathcal{O}(0.01)$ (Fearnhead, 1975; Schumacher et al., 1979)), $\langle |\boldsymbol{u}| \rangle$ is time-averaged horizontal speed of the flow, β_S is the saline contraction coefficient (8 x 10^{-4} g kg^{-1}), S is the water's salinity (assumed uniform), and h is the ocean cavity height. The critical melt rate, according to this formulation, was 1-4 mm yr^{-1} using the observed ML current speed (mean – 1 S.D. and mean + 1 S.D., respectively, from ADCP2), water column height, ML salinity, α = 0.01, and c_d = 0.003. While this critical melt rate estimate falls well below the observed melt rate of 5 ± 2 cm yr^{-1}, as expected for a stratified setting, we are unable to rigorously evaluate this formulation given uncertainties in c_d, $\boldsymbol{u}$, and α. This critical melt rate estimate is reduced from MacAyeal's (1984) estimate of ~1 m yr^{-1} for the Whillans Ice Stream grounding zone region, which likely resulted from overestimated current speeds as well as limited knowledge of ocean cavity geometry.

This analysis concurs with Holland (2008) that tidally-mixed zones do not form below the RIS in the presence of weak currents (~1 cm s^{-1}). A tidally-mixed zone may form in locations with larger tidal currents. The absence of significant tidal variations in current velocity contrasts with sub-ice-shelf settings that have tidal variations in current velocity that exceed the mean current (Nicholls et al., 1997). Our finding supports recent results from ocean circulation models that tidal currents may be spatially variable below ice shelves (Mueller et al., 2018).

Tidally-mixed zones are expected to freshen the inflowing water mass by mixing with the meltwater-influenced ISW. It is implausible that a tidally-mixed zone is present immediately seaward of this site given the highly saline water present at the borehole site. ML and BBL have salinities of 34.87 ± 0.01 g kg^{-1} and 34.88 ± 0.01 g kg^{-1}, respectively, which is more saline than 95% of HSSW by volume in the open Ross Sea (Orsi & Wiederwohl, 2009). While ML and BBL may be sourced from highly saline HSSW which is freshened by a tidally-mixed zone, a more plausible scenario is that ML and BBL are part of a continuous, inflowing HSSW, uninterrupted by full-water-column tidal mixing seaward of the borehole (Figure 7).

The absence of a tidally-mixed zone allows a buoyant upper layer or meltwater plume to develop at the grounding zone rather than 10s of km seaward outside a tidally-mixed zone. This difference in plume extent may result in a difference in plume velocity by controlling the distance over which the plume accelerates along a sloped ice-shelf base. Tidally-mixed zones may also alter plume buoyancy by controlling the distribution of meltwater. The absence of a tidally-mixed zone also allows dense seawater to reach the grounding zone without significant mixing with meltwater. Consequently, future changes in the temperature and salinity characteristics of that seawater may affect melt rates near the grounding zone more strongly in the absence of a tidally-mixed zone. The extent of tidally-mixed zones may be dynamically important below Antarctic ice shelves threatened by the intrusion of warm ocean water, by determining whether warm water masses can cause high melt rates at the grounding zone.

4.3 Contributions to vertical mixing

4.3.a. Shear-driven mixing

Turbulent eddies produced by boundary shear are likely to play a role in generating the observed three-layer structure. Temperature and salinity gradients tend to be homogenized within boundary layers through these eddies (e.g., Armi & Millard, 1976). The relative thicknesses of UL and the BBL are consistent with observationally-constrained scaling relationships for boundary layers. In a neutrally stratified water column with no buoyancy forcing, boundary layer thickness h is estimated to be $0.7u_*/f$, where f is the Coriolis parameter and u_* is the friction velocity (McWilliams & Huckle, 2006). For u_* determined by a quadratic drag law with c_D= 0.003 and a mean velocity of 1 cm s^{-1}, the neutral boundary layer is 3 m thick, consistent with the scale of the BBL.

The buoyancy flux provided by ice melting is expected to reduce the scale of eddies and thus reduce the scale of the ice-ocean boundary layer relative to a neutrally stratified boundary layer (McPhee, 1981). According to the analytic similarity theory extended by McPhee (1981) to the ice-ocean boundary layer, the boundary layer thickness scales with a stability parameter η_*: $h = c\eta_* u_*/f$, where c is about 0.5 and $\eta_* < 1$ (McPhee, 1981). For the buoyancy flux given by the observed melt rate (5 cm yr^{-1}, $\eta_* = 0.4$), the predicted ice-ocean boundary layer thickness is 1 m, similar to the observed UL. The details of this theory may not be entirely appropriate at the borehole site, where boundary layers were significantly thinner than the atmospheric and oceanic boundary layers for which the theory was developed. Nonetheless, the fact that UL is thinner than BBL is consistent with the hypothesis that boundary shear contributes to vertical mixing at the borehole.

Similar 3-layer stratification was observed near the grounding zone of Langhovde Glacier (Sugiyama et al., 2014). Two boreholes there revealed that horizontal velocities of 2-3 cm s^{-1} at both sites generated ~5 m thick boundary layers in one 24 m thick ocean cavity setting and fully mixed waters in a 10 m thick ocean cavity setting (Sugiyama et al., 2014). Although the ocean cavity studied here is thinner, velocities of ~1 cm s^{-1} may be fast enough to generate well-mixed boundary layers while being slow enough to permit stratification.

Given the low melt rates at this site, shear-driven mixing is not strong in the UL. This may change during periods of subglacial water discharge (Jenkins, 2011). The thin (1 m) UL and its high salinity indicate that high subglacial water discharge did not occur at the time of our observations. Subglacial Lake Whillans may episodically drain to the apex of this grounding zone embayment (Carter & Fricker, 2012), but a lake drainage had just occurred prior to our observations (Siegfried et al., 2016). The low melt rates at the borehole contrast with high melt rates (>10 m yr^{-1}) at nearby sites where high subglacial water discharge was inferred (Marsh et al., 2016).

4.3.b. Diffusive convection

Current forcing in this setting is low, both in the ML and likely also in the UL based on the low observed melt rates. This raises the possibility that double-diffusive convection contributes to vertical mixing. Ice-shelf melting can create the conditions for double diffusion by generating both a stable salinity gradient (by releasing freshwater) and an unstable temperature gradient (by extracting latent heat for melting). This unstable temperature gradient is a source of gravitational potential energy that can be released through diffusive convection when thermal diffusion produces instabilities at the edges of salinity interfaces (Radko, 2013). Turner angles (Figure 3) and the inverse stability ratio (Table 2) indicate that the observed stratification near the stable limit of the double-diffusive regime. Although

double-diffusive staircases can persist in the lab in the absence of shear up to $R_\rho^* = 55$ (Newell, 1984), canonically, stratification is considered prone to diffusive convection when R_ρ^* falls between 1 and 10 (Turner, 1965). R_ρ^* at this site is 8-10 between UL and ML and 3-5 between ML and BBL.

In Section 3.1 we found that the T-S trend in the UL was consistent with different effective diffusivities for heat and salt ($k_s/k_t < 1$) rather than fully turbulent. Unequal effective diffusivities in this sense is characteristic of double-diffusive regimes (Turner, 1965). Diffusive convection thus results in a low flux ratio, $c_{p,w}\beta q_s/\alpha q_t \cong 0.1$ (Kelley, 1990; Linden & Shirtcliffe, 1978; Turner, 1965). In contrast, if the water column were fully turbulent, the flux ratio for this setting between UL and ML would be 9. Thus, diffusive convection could have a profound impact on UL evolution. While the poor fit between observations and the meltwater mixing line may be an expression of diffusive convection, it could also be an expression of differential diffusion in the absence of diffusive convection (e.g., Merryfield, 2002) or lateral advection, and we do not have the observations to discriminate between these possibilities. Diffusive convection can produce well-mixed layers separated by interfaces with steep gradients in temperature and salinity, a stratification structure called a double-diffusive staircase. Double-diffusive staircases have been observed in the Arctic Ocean, driven by freshwater flux and cooling at the surface (Sirevaag & Fer, 2012); in lakes, driven by high geothermal heat flux at lake bottom (Sommer et al., 2013); and in one case below an ice shelf, driven by ice-shelf melting (Kimura et al., 2015). The observed stratification differs from typical double-diffusive staircases in having a larger temperature step (σ(0.1) °C compared with σ(0.001) - σ(0.01) °C) and salinity step (σ(0.1) g kg^{-1} compared with σ(0.001) - σ(0.01) g kg^{-1}) between UL and ML and thicker interfaces (σ(1) m compared with σ(0.1) m) (Padman & Dillon, 1987, 1988; Sirevaag & Fer, 2012; Sommer et al., 2013; Timmermans et al., 2008). The absence of a well-developed double-diffusive staircase may be related to high R_ρ^* values and large temperature and salinity gradients, which are associated with thicker interfaces (Marmorino & Caldwell, 1976; Newell, 1984; Sommer et al., 2013), or shear-driven mixing (Guthrie et al., 2017).

Shear-driven mixing may dominate heat and salt fluxes over double-diffusive convection at high R_ρ^* values (Crapper, 1976). Melt rates of 60 cm yr^{-1} observed 10 km from the grounding zone suggest that further up-shelf from the grounding zone shear-driven mixing dominates over molecular double-diffusion, indicating a limited double-diffusive zone. Although our analysis indicates that stratification at the Whillans Ice Stream grounding zone is marginally double-diffusive, this is due in part to the high salinity of the inflowing ML. Along other portions of the grounding zone that receive less salty HSSW or Low Salinity Shelf Water (Orsi & Wiederwohl, 2009), stability ratios may be lower and diffusive convection may be an important contribution to vertical mixing in quiescent grounding zone settings.

Where diffusive convection contributes to vertical mixing below ice shelves, it can have several important consequences for ice-shelf melting. Diffusive convection may play a significant role in plume evolution, as it fluxes buoyancy up vertical buoyancy gradients, in contrast to shear-driven mixing, which transports buoyancy down-gradient (Radko, 2013). In doing so, it may result in fresher ice-ocean boundary layers with lower thermal driving than may be present in shear-dominated regimes. Furthermore, double-diffusive fluxes are highly

sensitive to the stability of stratification. Laboratory experiments on double-diffusive staircases (Flanagan et al., 2013; Guo et al., 2018; Kelley, 1990; Marmorino & Caldwell, 1976; Turner, 1965) predict a power-law or exponential increase in heat fluxes as stability ratios decrease. Ongoing freshening and warming of HSSW (Jacobs & Giulivi, 2010) may decrease the stability of stratification at the RIS grounding zone and increase double-diffusive heat fluxes. The equilibrium response to such a perturbation is unknown, as it requires predictions of circulation patterns, the double-diffusive response, and ice-shelf melting. Predicting the sensitivity of ice-shelf melting to future ocean conditions may require a more thorough understanding of double-diffusive dynamics in sub-ice-shelf settings.

5 Conclusions

We collected contemporaneous oceanographic data through an ice borehole and measured basal melt rates of the RIS within a few kilometers of the grounding zone. This setting is characterized by low thermal driving (<0.1 °C) and low current forcing (~1 cm s^{-1}) compared with other ice shelves, where thermal driving at grounding zones often ranges from 0.5 - 4 °C (Rignot & Jacobs, 2002) and sub-ice-shelf current velocities are typically on the order of 10s cm s^{-1} (e.g., Nicholls et al., 2001). Basal melt rates in this grounding zone embayment were less than average for the RIS (Moholdt et al., 2014; Rignot et al., 2013) and are consistent with low shear stress at the ice-shelf base. Horizontal velocities within the 10 m thick sub-ice-shelf ocean cavity were on the order of 1 cm s^{-1} and did not experience significant tidal fluctuations. These weak currents did not generate a tidally-mixed zone at this portion of the grounding zone and allowed stratification to develop at the grounding zone. Since subglacial water discharge that enhances shear-driven boundary-layer mixing may be focused by channels (Le Brocq et al., 2013; Marsh et al., 2016) or be episodic (Siegfried et al., 2016) this low shear regime may be typical of many grounding zone settings.

The dynamics of vertical mixing are important for our understanding of the heat and salt fluxes that drive ice-shelf melting. Well-mixed layers within a few meters of the ice-shelf base and the seafloor suggest that boundary shear contributes to vertical mixing. Given low current velocities and favorable temperature and salinity gradients, diffusive convection may also be important. Ice-shelf melting can provide conditions favorable for diffusive convection by providing a flux of freshwater and extracting heat. Conditions are favorable for diffusive convection in 14% of the world's oceans (You, 2002), but the extent to which diffusive convection controls heat and salt fluxes in sub-ice-shelf cavities is unknown. Our understanding of the relationship between diffusive convection and current shear must be improved to assess the role of diffusive convection in ice-shelf cavities (Carpenter & Timmermans, 2014; Radko, 2016).

Acknowledgments, Samples, and Data

This material is based upon work supported by the US National Science Foundation, Section for Antarctic Sciences, Antarctic Integrated System Science program as part of the interdisciplinary WISSARD (Whillans Ice Stream Subglacial Access Research Drilling) project. Additional funding for instrumentation development was provided by grants from the Gordon and Betty Moore Foundation, the National Aeronautics and Space Administration (Astrobiology and Cryospheric Sciences programs) and the US National Oceanic and Atmospheric Administration. We are particularly thankful to the entire drilling team from the University of Nebraska–Lincoln and the WISSARD traverse personnel for crucial technical and logistical support. The United States Antarctic Program enabled our fieldwork, and New York Air National Guard and Kenn Borek Air provided air support. We acknowledge Keith Nicholls and Hugh Corr of the British Antarctic Survey for design and loan of the ApRES instrument and Timour Radko for helpful comments on the analysis of the observed double-diffusive staircase. C.B.B. was supported by the National Science Foundation Graduate Research Fellowship. M.A.K. is a recipient of an Australian Research Council Future Fellowship (project number FT110100207) and his research was supported under Australian Research Council's Special Research Initiative for Antarctic Gateway Partnership (Project ID SR140300001). M.R.S. was supported by NSF-ANT-0838885 and the George Thompson Postdoctoral Fellowship and Stanford University. This research is based on data services provided by the UNAVCO Facility with support from the National Science Foundation (NSF) and National Aeronautics and Space Administration (NASA) under NSF Cooperative Agreement No. EAR-0735156.

The authors declare no competing financial interests.

Basal melt rates and associated strain rates are available in the U.S. Antarctic Program Data Center, doi:10.15784/601122. Current velocity data and CTD data are available in the National Centers for Environmental Information, Accession Number 0176082. GPS data is available in the UNAVCO Data Center, doi:10.7283/T53R0RPD.

References

Table 1. Weekly basal melt rates at the WGZ borehole (GZ04).

Start Time (UTC)	End Time (UTC)	Interval [yr]	Melt [m]	Melt rate (m yr^{-1})	Vertical strain rates [10^{-4} yr^{-1}]
12 Dec 2014 01:15	21 Dec 2014 03:30	0.022	0.0019	0.086 ± 0.044	-0.1 ± 0.5
21 Dec 2014 03:30	30 Dec 2014 23:04	0.027	0.0015	0.055 ± 0.027	1.5 ± 0.3
30 Dec 2014 23:04	05 Jan 2015 04:00	0.014	0.0022	0.153 ± 0.061	0.4 ± 0.7
05 Jan 2015 04:00	20 Jan 2015 00:08	0.041	0.0021	0.053 ± 0.023	-1.0 ± 0.3

Note: Basal melt rates and vertical strain rates expressed as mean ± 1 S.D.

Table 2. Oceanographic conditions derived from CTD instrument.

	CTD Cast 1	CTD Cast 2*	CTD Cast 3
Background thermal gradient [°C m^{-1}]	0.031	0.035	0.033
UL temperature [°C]	-2.281 ± 0.005 †	-2.304 ± 0.006	-2.296 ± 0.006
UL salinity [g kg^{-1}]	34.74 ± 0.35 †	34.72 ± 0.02	34.74 ± 0.02
ML temperature [°C]	-2.036 ± 0.006	-2.050 ± 0.011	-2.010 ± 0.010
ML salinity [g kg^{-1}]	34.873 ± 0.006	34.865 ± 0.009	34.869 ± 0.007
BBL temperature [°C]	-1.972 ± 0.008	-1.975 ± 0.007	-1.963 ± 0.005
BBL salinity [g kg^{-1}]	34.882 ± 0.006	34.884 ± 0.007	34.883 ± 0.006
UL thickness [m]	0.8	1.2	0.7
UL-ML interface thickness [m]	2.9	2.5	2.5
ML thickness [m]	2.9	3.1	3.8
ML-BBL interface thickness [m]	1.2	1.2	2.5
BBL thickness [m]	2.0	1.8	0.9
R_ρ^* of UL-ML interface [ND]	--	10.1 ± 1.7	8.0 ± 1.1
R_ρ^* of ML-BL interface [ND]	2.5 ± 2.2	4.3 ± 2.8	5.1 ± 3.4

Note: Temperature and salinity standard deviations are determined by the variance of the values in each cast and the measurement error. Inverse stability ratio (R_ρ^*) standard deviations are determined by Gaussian propagation of errors from temperature and salinity errors.

* High frequency variability in CTD2 due to slow descent rates.

† Contamination by borehole water.

Table 3. Flux parameterizations for observed conditions at the WGZ borehole.

	Inferred from observed melt rate	*2-equation parameterizations*		*3-equation parameterizations*			
		MP99	J10	HO	KY (u_*)	MP (u_*)	J10 (u_*)
Heat flux [W m^{-2}]	0.49 ± 0.20	--	--	7.3	2.3	0.37	1.7
Salt flux [µg s^{-1} m^{-2}]	56 ± 22	--	--	723	230	37	170
Stanton number $c_d^{1/2}\Gamma_{\{TS\}}$ x 10^{-4}	0.87 ± 0.44	50-60	5.9	--	--	--	--
Inferred IO salinity [g kg^{-1}]	--	--	--	33.3	34.1	33.4	34.0
Melt rate [m yr^{-1}], UL inputs (mixing line inputs)	0.05 ± 0.02	--	--	0.66 (0.80)	0.21 (0.26)	0.034 (0.039)	0.15 (0.18)
Inferred friction velocity [m s^{-1}]	--	--	--	--	0.00016	0.001	0.00023
Inferred drag coef. for u = 1 cm s^{-1} [10^{-3}]	--	--	--	--	0.2	7	0.3
Inferred velocity for c_d = 0.001 - 0.01 [m s^{-1}]	--	--	--	--	0.0016 – 0.0051	0.010 – 0.032	0.0023 – 0.0072

Note: The exchange velocities associated with the melt rate observation use the observed ice-ocean salinity range. Fluxes are defined as positive upward. Exchange velocity parameterizations: HO = Hellmer and Olbers (1989), KY = Kader and Yaglom (1972), MP = McPhee (1983), J10 = Jenkins et al. (2010).

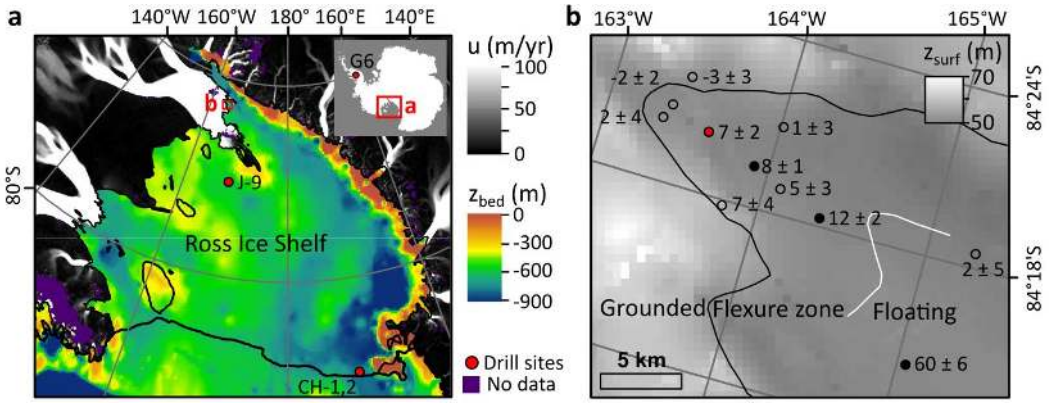

Figure 1. Measurement sites. **a.** Ross Sea region of Antarctica (inset). Bathymetry (z_{bed}) is shown for the Ross Sea (Fretwell et al., 2013). Grounded ice velocity (u) (Rignot et al., 2011) is shown by grey shading. The RIS is outlined in black (Rignot et al., 2011). Red circles indicate locations of oceanographic observations below the RIS (CH-1,2: Arzeno et al., 2014; J-9: Jacobs et al., 1979) and the George VI Ice Shelf (G6: Kimura et al., 2015). **b.** Locations of radar measurements (black circles) with mean melt rate ± 1 S.D. (cm yr^{-1}) on an ice surface elevation model ($z_{surface}$) (DiMarzio, 2007). Empty circles indicate melt rates within 2 S.D. of 0 cm yr^{-1}. The borehole is highlighted in red. Inland and seaward limits of the flexure zone are shown with black and white lines, respectively (Marsh et al., 2016).

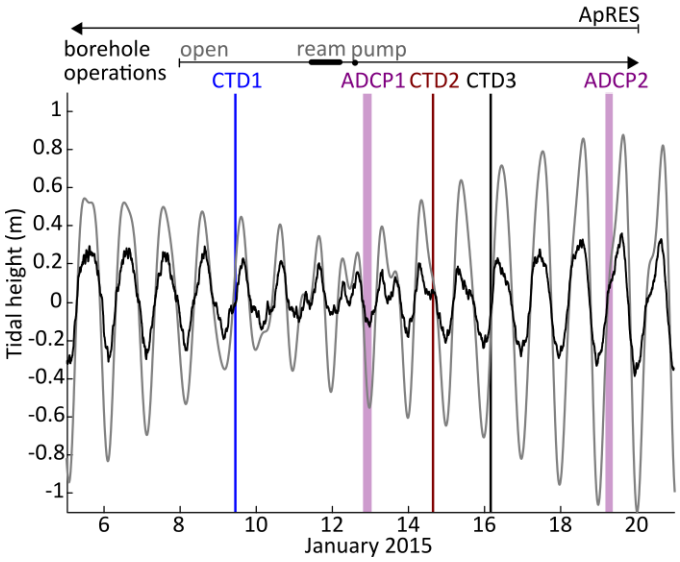

Figure 2. Timeline of observations. ApRES measurement period at the borehole starting on December 13, 2014 (top horizontal line). Operations began with borehole opening to the ocean (thin vertical line) and include reaming with hot water (thick horizontal line) and withdrawal of borehole water by pumping (starting at the black dot). Borehole instrument deployments (vertical lines) include three CTD casts and two ADCP measurements. GPS height data at borehole (black) are compared with the CATS2008a tide model (grey) (after Padman et al., 2002).

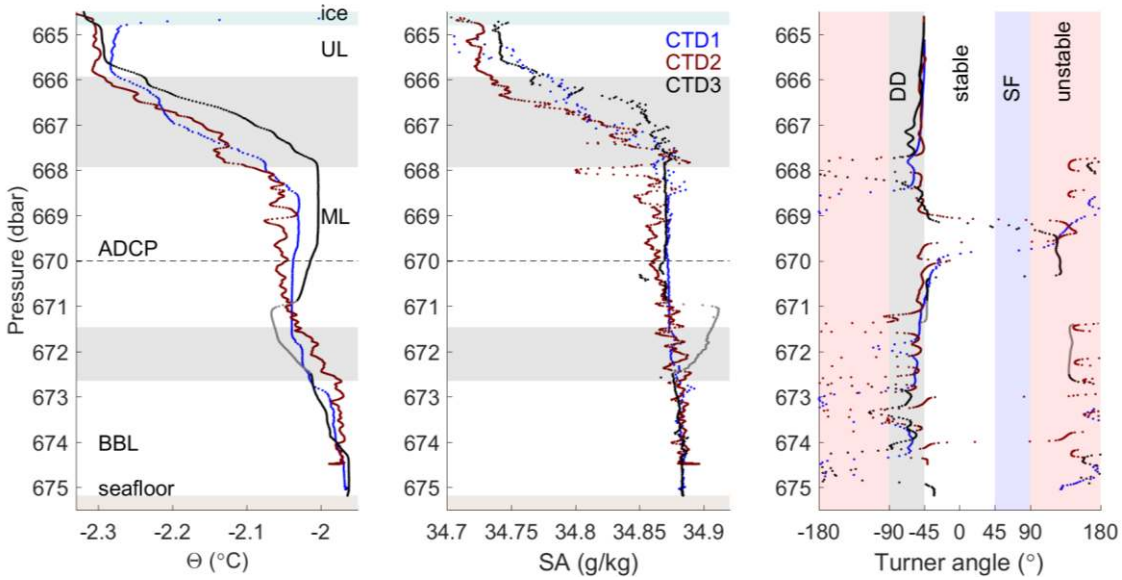

Figure 3. CTD observations. **a,b.** Unfiltered data (points) for (a) conservative temperature (Θ), (b) absolute salinity (SA). Individual casts are numbered, corresponding to the timeline given in Figure 2. The UL of CTD1 is warmed and freshened by borehole water. A segment of CTD3 (grey) is affected by a temperature sensor malfunction, which is propagated to Θ and SA. Mixed layers are shown without shading and interfaces with grey shading. Dashed horizontal line shows the approximate depth of the ADCP instrument. **c.** Turner angle for filtered CTD data. Stratification regimes are shaded and labeled (DD = double-diffusive regime, statically stable regime, SF = salt fingering regime, statically unstable regime).

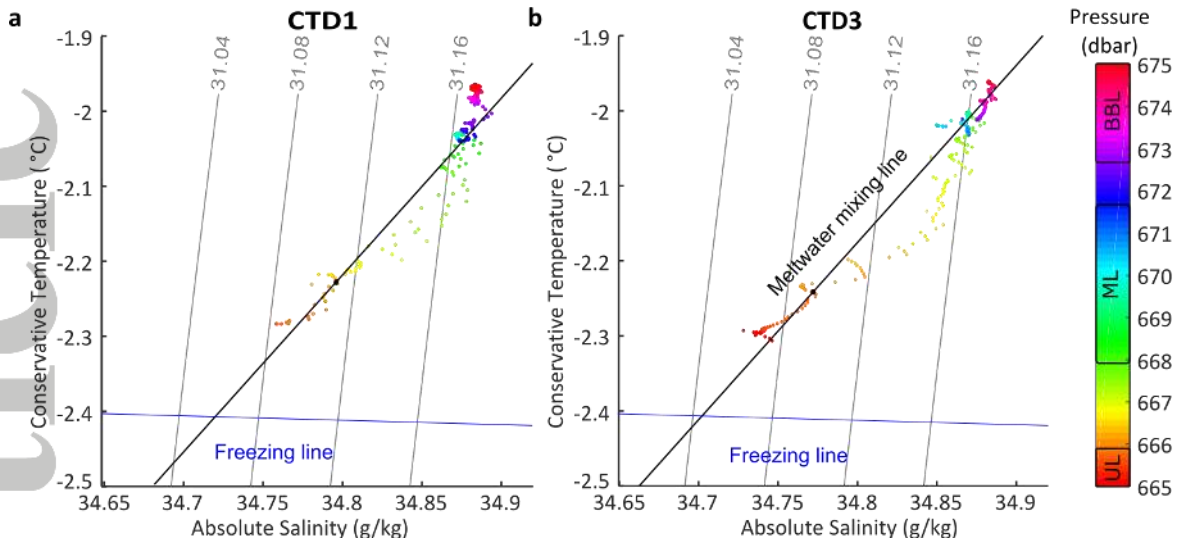

Figure 4. Temperature-salinity plots for Cast 1 (a) and Cast 3 (b). Data in the UL from Cast 1 are omitted due to contamination with borehole water. Unfiltered CTD data is coloured by the pressure at which it was collected. Lines of constant density are plotted in grey. Freezing line (blue) is plotted for a constant pressure of 665 dbar. **b**. The meltwater mixing lines is plotted in black, and a black point along that line denotes the source water chosen.

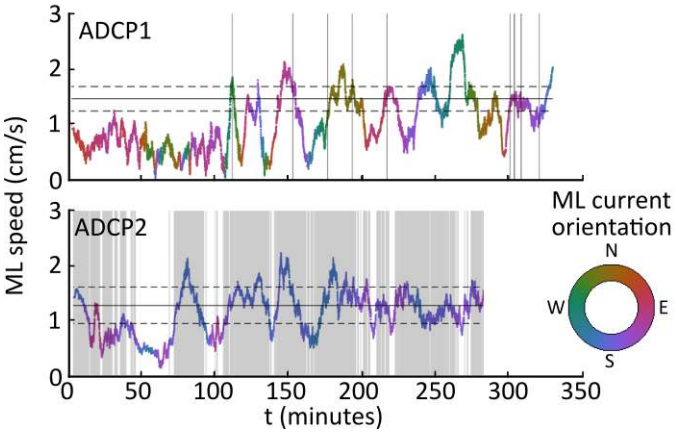

Figure 5. Current speed and orientation (color) at 5 m depth in the sub-ice shelf ocean cavity within the Middle Layer (ML). Mean current speed ± 1 S.D. are indicated (horizontal lines). Data analysis windows are shaded; see Figure 2 for time period of observations.

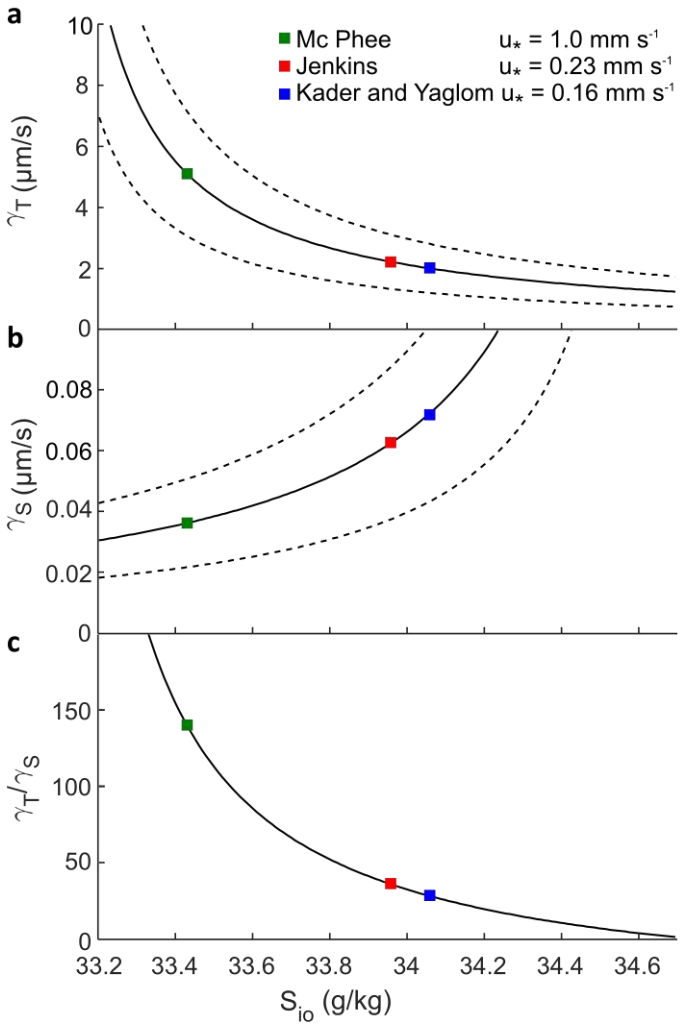

Figure 6. Solutions to the 3-equation formulation for the observed melt rate at the borehole. Solutions corresponding to the mean melt rate fall along the black solid line; dotted lines bracket 2 S.D. of the melt rate. Sensitivity of (a) heat exchange velocity (γ_T) and (b) salt exchange velocity (γ_S) and (c) the ratio of heat exchange velocity to salt exchange velocity (γ_T/γ_S) to the salinity at the ice-ocean interface (S_{io}). The grey shaded interval spans salinities observed at the base of the ice borehole, taken to be upper bounds on S_{io}. Colored squares correspond to parameterized exchange velocities at the friction velocity required to reproduce the mean melt rate.

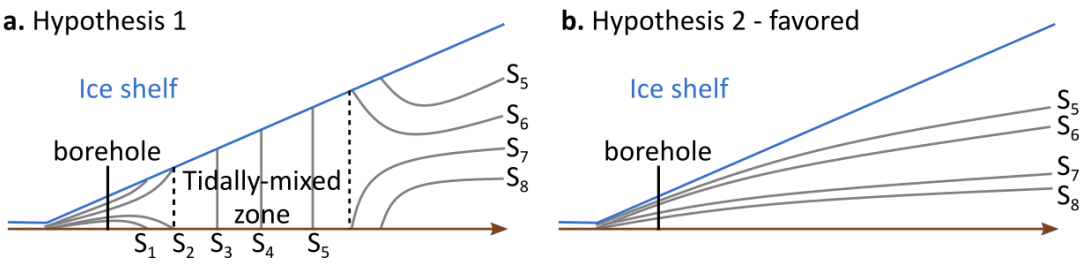

Figure 7. Schematic of the sub-ice shelf cavity (a) with a tidally-mixed zone and (b) without a tidally-mixed zone. Grey lines represent schematic isopycnals. Salinities increase as subscripts increase. Dashed black lines mark the limits of the tidally-mixed zone, after Holland (2008).